Spatially and Kinetically Resolved Mapping of Hydrogen in a Twinning-Induced Plasticity Steel by Use of Scanning Kelvin Probe Force Microscopy

Motomichi Koyama,[a,b,z] Asif Bashir,[a,c,z] Michael Rohwerder,[a,c,*] Sergiy V. Merzlikin,[a,c] Eiji Akiyama,[d] Kaneaki Tsuzaki,[b,d] and Dierk Raabe[a]

[a]*Max-Planck-Institut für Eisenforschung GmbH, 40237 Düsseldorf, Germany*
[b]*Department of Mechanical Engineering, Kyushu University, Nishi-ku, Fukuoka 819-0395, Japan*
[c]*Christian Doppler Laboratory for Diffusion and Segregation Mechanisms, 40237 Düsseldorf, Germany*
[d]*National Institute for Materials Science, Ibaraki 305-0047, Japan*

The hydrogen distribution in a hydrogen-charged Fe-18Mn-1.2C (wt%) twinning-induced plasticity austenitic steel was studied by Scanning Kelvin Probe Force Microscopy (SKPFM). We observed that 1–2 days after the hydrogen-charging, hydrogen showed a higher activity at twin boundaries than inside the matrix. This result indicates that hydrogen at the twin boundaries is diffusible at room temperature, although the twin boundaries act as deeper trap sites compared to typical diffusible hydrogen trap sites such as dislocations. After about 2 weeks the hydrogen activity in the twin boundaries dropped and was indistinguishable from that in the matrix. These SKPFM results were supported by thermal desorption spectrometry and scanning electron microscopic observations of deformation-induced surface cracking parallel to deformation twin boundaries. With this joint approach, two main challenges in the field of hydrogen embrittlement research can be overcome, namely, the detection of hydrogen with high local and chemical sensitivity and the microstructure-dependent and spatially resolved observation of the kinetics of hydrogen desorption.
© 2015 The Electrochemical Society. [DOI: 10.1149/2.0131512jes] All rights reserved.

Hydrogen embrittlement of austenitic steels is of high interest because of the potential use of these materials in hydrogen-energy-related infrastructures.[1–5] In order to elucidate the associated hydrogen embrittlement mechanisms, the mapping of heterogeneities in strain,[6,7] damage (crack/void),[8] and hydrogen[9,10] and their relation to the underlying microstructures is a key assignment in this field. Specifically mapping the connection between microstructure heterogeneity and the associated hydrogen trapping at similar spatial resolution opens a novel pathway to identify hydrogen embrittlement mechanisms in complex alloys.

One of the materials classes that is expected to be applied for energy-related structure parts are austenitic steels with high Mn content.[3,11] In particular, twinning-induced plasticity (TWIP) high Mn austenitic steels are well known for an exceptional balance of ductility and strength with less hydrogen susceptibility compared to ferritic steels with a similar strength.[12–14] The hydrogen embrittlement phenomenon has been observed under severe mechanical deformation and hydrogen charging conditions such as delayed fracture testing in a deep drawn cup or tensile testing during hydrogen charging at a high current density.[15–17] Fracture was in such cases caused by various metallurgical factors e.g. by the formation and failure of deformation twins.[3,18] The importance of deformation twins on hydrogen embrittlement of austenitic steels has been recently studied.[3,18–21] It was found that they can act as crack initiation sites and enable crack propagation.[3,18–20] Microstructure-sensitive hydrogen mapping in a TWIP steel has been conducted by using microprinting experiments,[19] which enable visualization of hydrogen emission from a sample through reduction of silver ions in gelatin-based AgBr emulsion.[22–24] The microprinting technique demonstrated that hydrogen is indeed localized at deformation twins, hence, promoting the initiation of hydrogen embrittlement.[19] Also, from our previous experiments we suggested that the hydrogen localization at/near deformation twins requires local plastic straining at/before deformation twins.[3] These facts indicate that the hydrogen-assisted twin boundary cracking of TWIP steels is a complex phenomenon including both, local plastic straining and local hydrogenation. To better understand the influence of deformation twins on the hydrogen embrittlement phenomenon, it is thus essential to map the spatial hydrogen distribution through a high resolution detection approach that is sufficiently microstructure and concentration sensitive. It should be noted here

that the microprinting technique is only sensitive to hydrogen at relatively high concentration levels, or more precisely at relatively high emission rates. It has, therefore, to be applied directly after a sample is charged with hydrogen. It will be shown here that hydrogen is critical for prolonged times after charging. Hence, the findings obtained by microprinting needed to be confirmed also for longer times after charging by a more sensitive technique.

In the last years several promising novel approaches have been reported for the localized resolved and sensitive detection of hydrogen. One is a direct electrochemical detection via a capillary cell, developed by Suter et al. (see e.g. Ref. 25), which, however, does not provide the resolution required here. Another approach is the use of Kelvin probe techniques, which allow detection of hydrogen in a material by means of the change of work function caused by the hydrogen entering the oxide at the surface (see e.g. discussions in Refs. 26 and 27). Studies at quite high resolution have been carried out with Scanning Kelvin Probe Force Microscopy (SKPFM), where diffusion profiles of hydrogen have been mapped successfully at relatively high resolution at cross section of samples after hydrogen charging.[28,29] However, a direct quantification is not possible by this method, due to the complex dependence of the work function of oxide on different defect states in the oxides (see discussion in Ref. 26). For the same reason this approach is not suitable to provide reliable information on hydrogen at different features of the microstructure, because different oxides show a different dependence on hydrogen.[26] A new approach by applying a thin palladium layer eliminates this problem. More specifically, the SKPFM with a thin palladium layer is a novel and efficient method to very sensitively analyze local hydrogen concentrations down to levels well below 0.01 atom ppm at spatial resolutions as small as several tens of nanometers.[30–32] The SKPFM can hence be used for detecting the hydrogen distribution with high sensitivity, since the potential measured by the SKPFM on the palladium that has been deposited as a thin layer on the hydrogen charged sample surface correlates logarithmically with the hydrogen content in the palladium.[26,33,34] Because of this Nernstian-like behavior, which is similar to a hydrogen electrode, as also reported for immersed palladium metal,[33] we also refer to the work function as electrode potential. In fact, as discussed previously,[26,30,34] the surface of the palladium is, even in dry nitrogen atmosphere, still covered by an ultrathin water layer, which together with the hydrogen in the palladium leads to the formation of an hydrogen electrode "in the dry".[34] By exploiting this effect, SKPFM was successfully applied to the spatially resolved detection of hydrogen in ferrite/austenite duplex stainless steels that were chemically etched and coated with a 100-nm-thin palladium

layer. Since the chemical potential of hydrogen in palladium is much lower than in the steel, diffusible hydrogen leaves the steel microstructure and gets locally stored in the palladium layer above it, causing a corresponding change in the work function.[26,34] Hence, this method is capable of clearly revealing a hydrogen-enhanced contrast in the potential between the two phases.[30] This means that the palladium layer acts as an accumulation and detection layer for hydrogen.

For the specific microstructure under investigation we have to consider that the crystal structure of the deformation twins is the same as that of the matrix.[35–37] The twin thickness (1–3 μm) in the current material is much smaller than the grain size of the duplex steel studied by this method before.[30] This means that the detection of the spatial hydrogen distribution in the matrix/deformation twin structure requires a higher hydrogen detection sensitivity than used before on other microstructures.

The current study thus aims at overcoming two main challenges in the field of hydrogen embrittlement research, namely, (1) detecting hydrogen at high local and chemical sensitivity at deformation twins on a palladium-coated layer without chemical etching; and (2) studying changes in the hydrogen distribution as a function of time associated with hydrogen desorption into the surrounding dry nitrogen atmosphere.

Experimental

Material synthesis and microstructure characterization.— A Fe-18Mn-1.2C steel (wt%) showing deformation twinning[14] was used. It was solution treated at 1273 K for 3600 s after forging and rolling at 1273 K. The average grain size was 46 μm including the annealing twin boundaries.[14] The steel shows no martensite even after fracture.[14] A plate specimen was cut by spark erosion. All specimens used in this study were tensile-strained to 30% to produce deformation twins. The details of the deformation microstructure and hydrogen embrittlement behavior of the present steel have been reported in previous studies.[3,14]

Electron backscatter diffraction pattern (EBSD) measurements were obtained on a specimen mechanically polished with colloidal silica. The microscope was operated at 20 kV with a beam step size of 300 nm (Figs. 1a and 1b) and 20 nm (Figs. 1c and 1d), respectively.
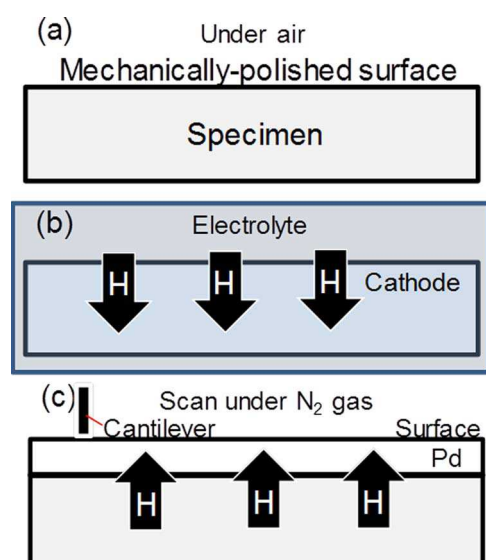

Figure 1. Schematics describing the sample preparation for conducting SKPFM (Scanning Kelvin Probe Force Microscopy). (a) Mechanical polishing for obtaining a flat surface. (b) Hydrogen charging to the mechanically-polished specimen. (c) SKPFM starts on the palladium-coated surface during hydrogen desorption from the specimen.

Determination of hydrogen trapping energies.— In order to determine the hydrogen trapping energy levels for the different types of lattice defects, thermal desorption analyses (TDA) were conducted from room temperature up to 800°C using a quadrupole mass spectrometer for the detection of hydrogen evolving from the 30% deformed specimen. The dimension of the specimen used for TDA was 15 mm × 15 mm × 0.5 mm. Cathodic hydrogen charging was performed on the mechanically polished surface at a voltage of −700 mV vs. Ag/AgCl for 30 min in a 0.9 M H_2SO_4 aqueous solution containing 3 g · L^{-1} of NH_4SCN. A platinum wire was used as counter electrode. 3 M solution was used for the Ag/AgCl reference electrode. The open circuit potential of the steel immersed in the acid solution was −0.4 V vs. the Ag/AgCl reference electrode. Since hydrogen is considered to localize in the vicinity of the specimen surface because of the short hydrogen charging time, one should note here that the desorption rates obtained in this study depend on the surface area. TDA was started within 25 min after the hydrogen charging. The heating rate was changed from 6 to 90 K · min^{-1} to estimate the activation energies for hydrogen desorption pertaining to a specific trap site distribution. The activation energies were estimated by using a Kissinger plot as defined in Ref. 38, i.e.

$$\frac{\partial ln\left(\frac{\varphi}{T_c^2}\right)}{\partial\left(\frac{1}{T_c}\right)} = -\frac{E_a}{R} \quad [1]$$

where φ is the heating rate, T_c the temperature in kelvin at which the maximum of the hydrogen desorption peak appears, R the gas constant, and E_a the activation energy for hydrogen desorption. The activation energies for hydrogen desorption from the different trap sites were calculated as the slope of a $ln(\varphi/T_c^2)$ vs $1/T_c$ plot. The obtained activation energies were then used to identify the active hydrogen trap sites.

Hydrogen mapping in conjunction with microstructure characterization.— The SKPFM measurements were carried out with an Agilent 5500 SPM device. The silicon based atomic force microscope tips were coated with Pt/Ti (20 nm) on the tip side and Al reflex coating at the back side and the tip radius was 28 ± 10 nm at the apex. The 30% deformed specimen investigated with the SKPFM was first lapped and subsequently buff-polished with colloidal silica for 30 minutes (Fig. 1a). Topographic features arising from deformation twins appear during the long time buff-polishing. Hydrogen was introduced into the polished specimens by electrochemical charging in the same condition used for the TDA (Fig. 1b). The hydrogen-charged specimen was covered by palladium with a thickness of 100 nm by means of physical vapor deposition (PVD). Altogether about 1 hour lapsed after charging with hydrogen before the desired condition is reached. Then, SKPFM observations were conducted on the specimen surface under dry nitrogen gas atmosphere (Fig. 1c). The dry nitrogen gas atmosphere suppresses the loss of hydrogen from the palladium by oxidation to water. The consecutive enrichment of hydrogen in the palladium, driven by the locally available diffusible hydrogen, results in the evolution of potential contrast in the SKPFM images.[26,34] One should note that even when the initial diffusible hydrogen is desorbed, new diffusible hydrogen is further supplied, although at low rates, from deeper trap sites.[26,34] These will, even a long time after hydrogen loading, still be actively releasing hydrogen close to the surface,[26,34] which leads to high achievable local resolution even after longer times. Such high resolution is made possible by the nano-crystalline character of the Pd film, which prevents fast lateral cross-diffusion of the hydrogen.[26,32]

Tensile testing and fractography.— Tensile tests were conducted at ambient temperature with and without hydrogen pre-charging in the same condition used for the TDA and SKPFM. The tensile tests with hydrogen pre-charging were started after exposure to air for 0, 6, and 67 h. In order to determine a strain rate of the present study, the following two factors were considered. 1) The strain rate is required to be as low as possible, since the competitive motion of hydrogen
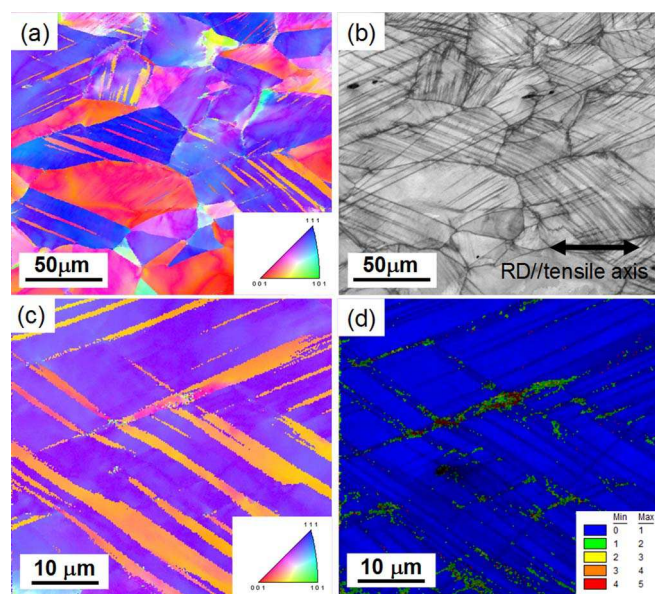
Figure 2. EBSD results obtained on the 30% pre-deformed specimen prior to hydrogen-charging. (a) RD-IPF and (b) IQ maps on a large area. (c) High resolution RD-IPF map. (d) KAM+IQ map showing the correspondence between deformation twin and strain localization. RD: rolling direction // tensile direction; IPF: inverse pole figure; IQ: image quality; KAM: Kernel average misorientation.

and dislocation is crucial for hydrogen-enhanced localized plasticity. 2) The total test time must be significantly shorter than 6 h to compare the results at the exposure times of 0 and 6 h. Because of these two reasons, the strain rate was selected to be 1.0×10^{-3} s^{-1}. Then, the sample surfaces (ND) and fracture surfaces (RD) were observed by scanning electron microscopy (SEM) to investigate the appearance of hydrogen-assisted cracking. The SEM was operated at an acceleration voltage of 20 kV.

Results

Preliminary experiments.— The initial microstructure in the 30% deformed specimen is shown in Fig. 2. The rolling direction (RD// tensile axis) inverse pole figure (IPF), and image quality (IQ) maps shown in Figs. 2a and 2b exhibit a considerable amount of deformation twins in most of the grains.[39] The high resolution RD-IPF map (Fig. 2c) shows that the thickness of the twin plates is 1–3 μm. Additionally,

geometrically necessary dislocation patterns formed during plastic straining at the deformation twin plates as revealed by the Kernel average misorientation map (Fig. 2d).

Figure 3 shows topographic and surface potential images of the buff-polished surface without hydrogen-charging and a palladium layer taken by SKPFM. The topography appearing during the buff-polishing with colloidal silica is attributed to a difference in hardness between matrix and deformation twin, since deformation twin plates include a considerable amount of lattice defects. Since a soft region is easier to polish compared to a hard region, the relatively-soft matrix and hard deformation twins appear as bright (higher position) and dark contrasts (lower position), respectively as shown in the topographic images of Fig. 3a′. These features match the deformation twin morphology observed by EBSD. Note that the potential image shown in Fig. 3b′ shows heterogeneity even without hydrogen-charging. The palladium coating on the specimen surface initially leads to a homogeneous potential on the sample surface, eliminating specifically potential difference effects associated with crystal orientation, second phases, and lattice defects as shown later.

Thermal desorption analysis.— Figure 4 shows examples of TDA results at heating rates of 6, 19.8, 60, and 90 K·min^{-1}. The TDA profiles can be deconvoluted into 5 peaks shown as broken curves. The respective peak positions shift to higher temperatures with increasing heating rate. Fig. 5a shows TDA profiles obtained (i) before hydrogen-charging, (ii) immediately after hydrogen-charging, and (iii) after hydrogen-charging and subsequent exposure to air for 300 h at room temperature. As shown here, the height of all peaks increased due to hydrogen-charging. Then, the first and second peaks in the temperature range between room temperature and ∼300°C totally disappeared after exposure to air for 300 h at room temperature. In particular, the first peak disappeared already after exposure for 6 h as shown in Fig. 5b. Additionally, the cumulative hydrogen content corresponding to the third peak decreased and reached the level observed for the hydrogen-uncharged specimen after an exposure for 300 h to air. On the other hand, the cumulative hydrogen amounts corresponding to the fourth and fifth peaks rather increased after air exposure for 300 h compared to the hydrogen amount observed immediately after the hydrogen-charging. More quantitatively, after the charging, the total hydrogen concentration of the samples was equal to 6.5 ± 1.0 wt ppm depending on the individual sample, with approx. 2 wt ppm being trapped and rest diffusible. After 6 h of the exposure to the ambient air, peak 1 evolved out of the sample, decreasing the concentration of the diffusible hydrogen by factor 1.7 (2.5 wt ppm remaining from 4.1 measured immediately after the charging of the similar specimen at the same heating rate). The sample stored during 300 h on air showed no peaks corresponding to diffusible hydrogen,
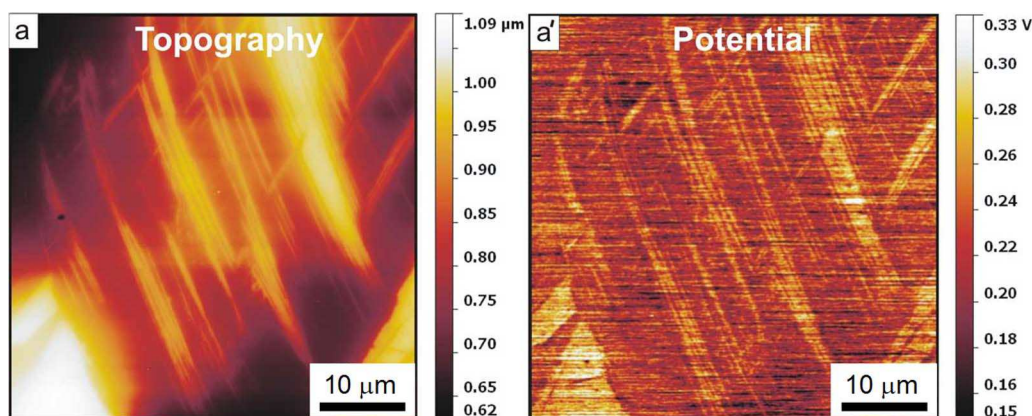

Figure 3. SKPFM data obtained on the specimen surface without palladium coating directly after mechanical polishing with colloidal silica. Topography and potential maps are shown in Fig. 3a and 3a′, respectively. The plates within the grain are deformation twins. This reference image reveals potential differences due to surface topography caused by twinning, phase contrast and dislocation patterning. These microstructure differences are eliminated once the sample is palladium-coated so that the effect of the evading hydrogen alone can be detected.
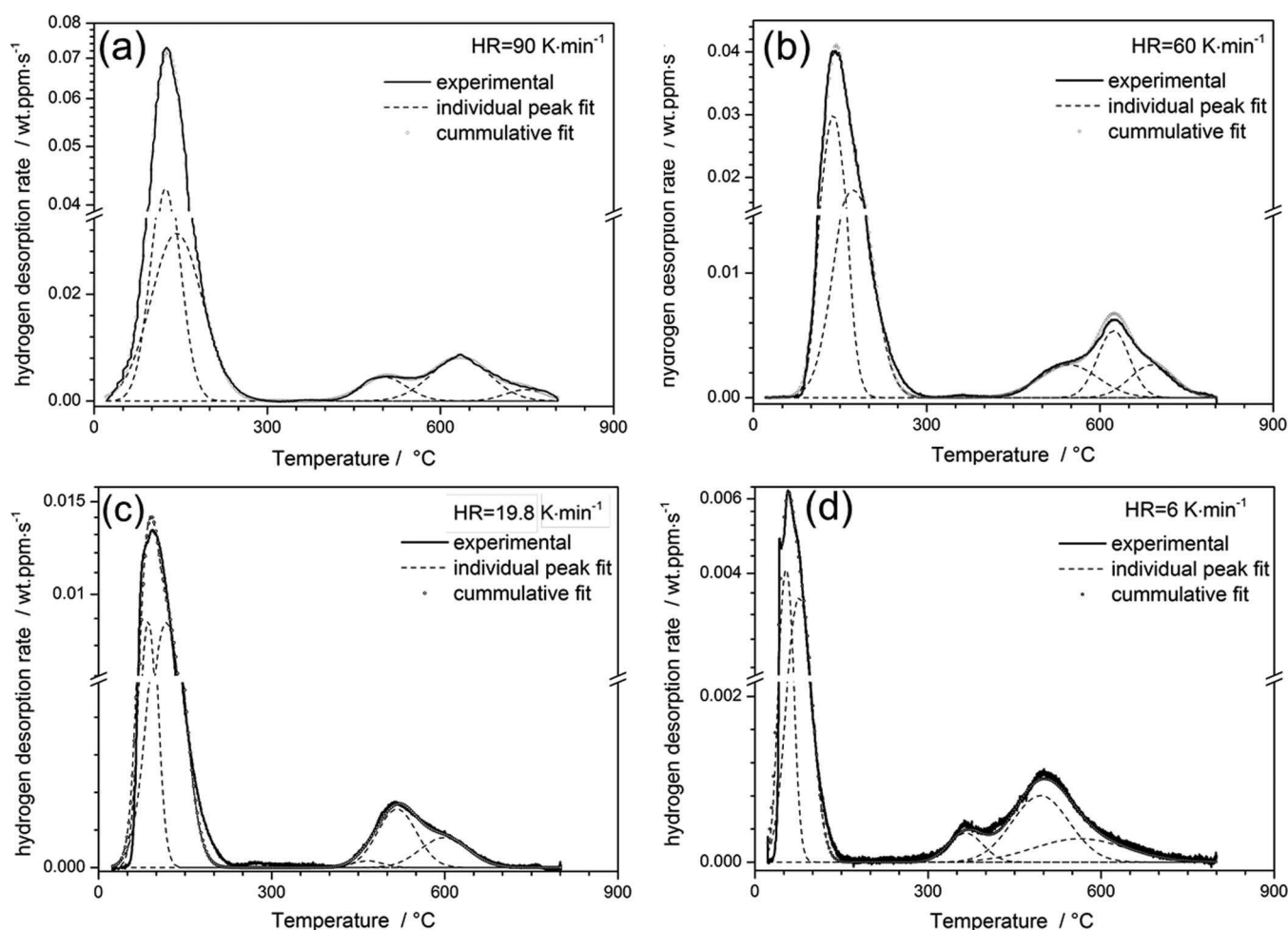
Figure 4. Hydrogen desorption rate curves at heating rates of (a) 90, (b) 60, (c) 19.8, (d) 6 K · min^{-1}.

but the amount of 2.3 wt ppm for hydrogen being trapped in the last 3 peaks.

Since the peaks in the TDA profiles shifted to higher temperature levels with increasing heating rate, the profiles can be used for a Kissinger analysis[38] in order to determine the activation energy for hydrogen detrapping as shown in Fig. 6. By using Eq. 1, the activation energies for the 1st-5th peaks were determined to be approximately 30, 32, 58, 71, and 80 kJ · mol^{-1}, respectively.

Scanning Kelvin Probe Force Microscopy.— Figure 7 shows the summary of the SKPFM measurements at various exposure times after hydrogen charging plus the subsequent palladium coating. The topographic images reveal primary and secondary deformation twin plates as indicated in Fig. 7a. These topographic features did not change during the measurements as revealed in Figs. 7a through 7e. In contrast, the work function, here referred to as electrode potential,[31,40] increased exponentially with exposure time from Figs. 7a′ to 7c′ similarly as reported previously.[40] The change in the work function was correlated with the presence of hydrogen, and had been quantitatively calibrated before to estimate the hydrogen content in palladium. The actual calibration curve is shown in Ref. 34. This calibration shows that the work function decreases with increasing hydrogen content, indicating that the microstructurally localized hydrogen is visualized in terms of dark contrast in the corresponding SKPFM potential maps. Figs. 7a′ through 7d′ reveal that the deformation twins are characterized by a distinct drop in the potential when compared to the matrix. This can be seen from the dark color at the locations where deformation twins exist, indicating a higher hydrogen uptake into the palladium at these

locations. Specifically, this effect can be observed at the positions indicated by arrows in Figs. 7b′ and 7c′.

Figure 8a shows the line profiles corresponding to the white lines in Figs. 7a′ to 7e′. The three dotted lines in Fig. 8a correspond to the locations of the deformation twins indicated by the black arrows in Fig. 7. The potential difference between twins and matrix is highest after an exposure time of 67 hours, and then it decreases with further exposure time. Fig. 8b shows the difference between the average potential of the matrix and the local potential at the deformation twins. The local potential at the deformation twins was defined as the average of the minimum potentials of the respective twins shown in Fig. 8a. The change in potential difference between twin and matrix more clearly demonstrates that the relative difference in potential increased with exposure time until 67 h and decreased with exposure time from 67 to 300 h, corresponding to the evolution and disappearance of dark contrast as a function of the exposure time to the dry nitrogen atmosphere shown in Fig. 7. This fact indicates the widening and then narrowing of the difference in hydrogen content between twin and matrix.

Tensile testing.— Figure 9 shows engineering stress-strain curves at different exposure times after hydrogen-charging for 30 min. The specimens after hydrogen charging were exposed to air at ambient temperature. The stress-strain responses and mechanical properties were not dependent on the exposure time to air after the preceding hydrogen charging.

Figure 10 shows fractograph images observed after the fracture shown in Fig. 9. In the hydrogen-uncharged specimen (Fig. 10a), the
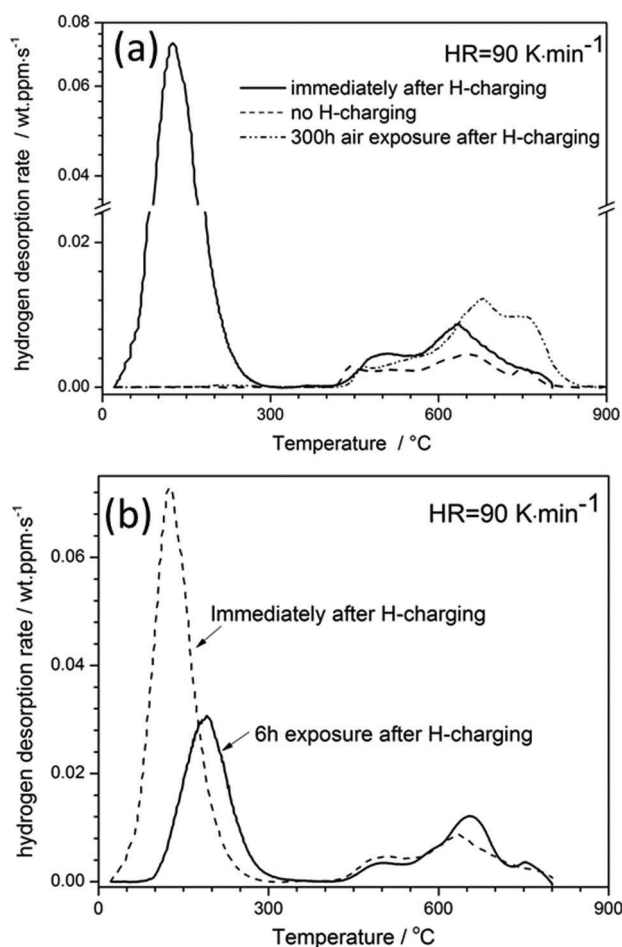
fracture surface was totally ductile. In the case studied immediately after hydrogen-charging (Fig. 10b), brittle fracture features were observed in the vicinity of the sample surface. The brittle features still remained even after the exposure to air for 6 h (Fig. 10c), although the total area affected by brittle fracture was reduced compared to Fig. 10b. Finally, the brittle fracture features entirely disappeared after an exposure at air for 67 h (Fig. 10d). The magnified images of the brittle features are shown in Figs. 11a and 11b. The brittle fracture features do not represent simple intergranular cracking but multiple steps and surface traces are observed too.

Figure 12 reveals surface cracks and voids in the fractured specimens. In the case without hydrogen charging, spherical voids formed at the austenite/inclusion interfaces as shown in Fig. 12a. On the other hand, the specimens studied immediately after hydrogen charging and after subsequent exposure to air for 6 h showed brittle cracks along or parallel to grain and twin boundaries as indicated by red and yellow arrows, respectively (Figs. 12b and 12c). The number frequencies of both, the grain and twin boundary cracking events decreased with increasing exposure time to air. In particular, the cracks formed along the grain boundaries propagated easily immediately after hydrogen-charging, and this fast propagation phenomenon was suppressed distinctly by the exposure to air. The brittle cracks totally disappeared, and voids which initiated from inclusions appeared again after 67 h of air exposure as shown in Fig. 12d. Here, an important difference between the uncharged specimen and the 300 h-exposed specimen should be noted, namely, slip traces along {111} were observed around the void shown in Fig. 12d.

Discussion

Hydrogen effects in TWIP steels have been discussed to affect dislocation mobility,[17,41] strain aging,[5,42,43] and the cohesive energy of grain boundaries.[15] The relative contribution of these factors is dependent on the micro-distribution of the hydrogen. The hydrogen segregation leads to hydrogen-assisted cracking in TWIP steels, specifically along grain[15,16,44] and $\Sigma 3$ twin boundaries.[3,18,19] The symbol Σ stands for the coincidence site lattice parameter describing the inverse frequency of atoms matching atomic positions that fit a joint superlattice, i.e. positions pertaining to both abutting crystals. A low Σ number,
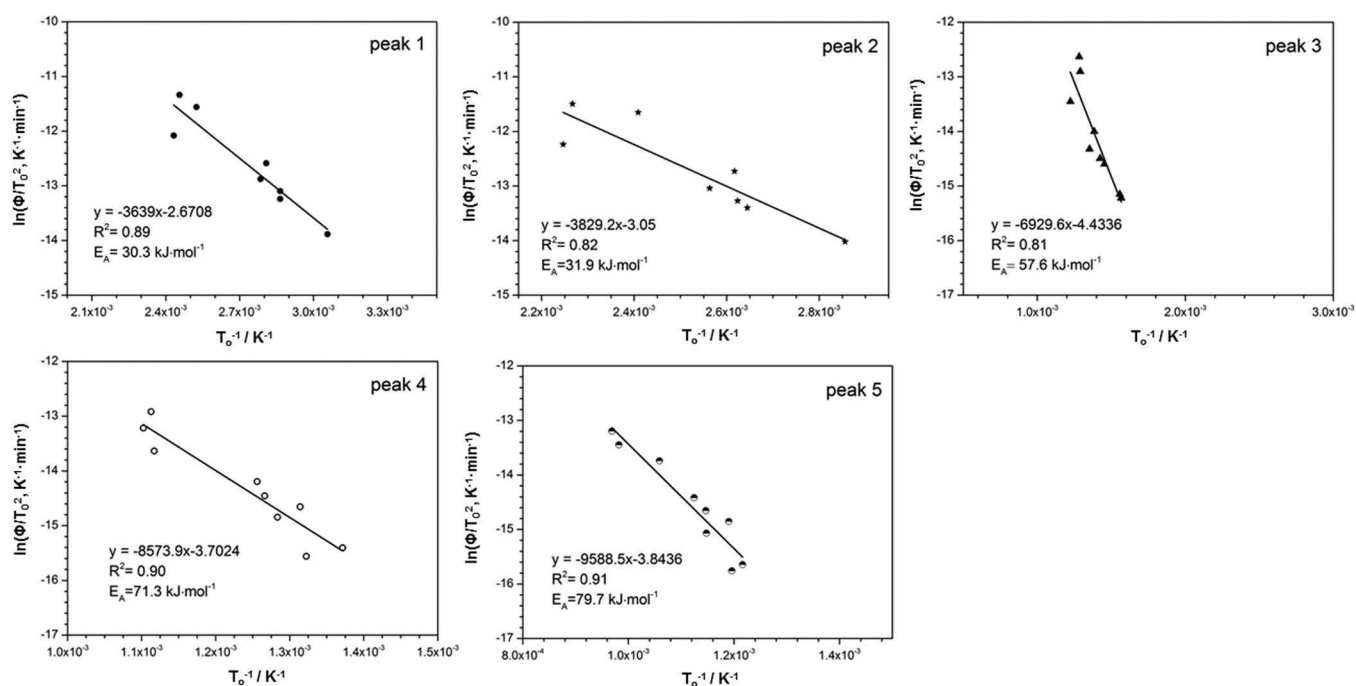
Figure 5. Hydrogen desorption rates plotted against temperature at a heating rate of 90 K·min^{-1} (a) before and after hydrogen charging, and after hydrogen-charging and subsequent exposure for 300 h. (b) The TDA profiles immediately after hydrogen-charging and after 6 h from hydrogen-charging. TDA: thermal desorption analysis.

Figure 6. Kissinger plots obtained from TDA including the results in Fig. 5. TDA: thermal desorption analysis.
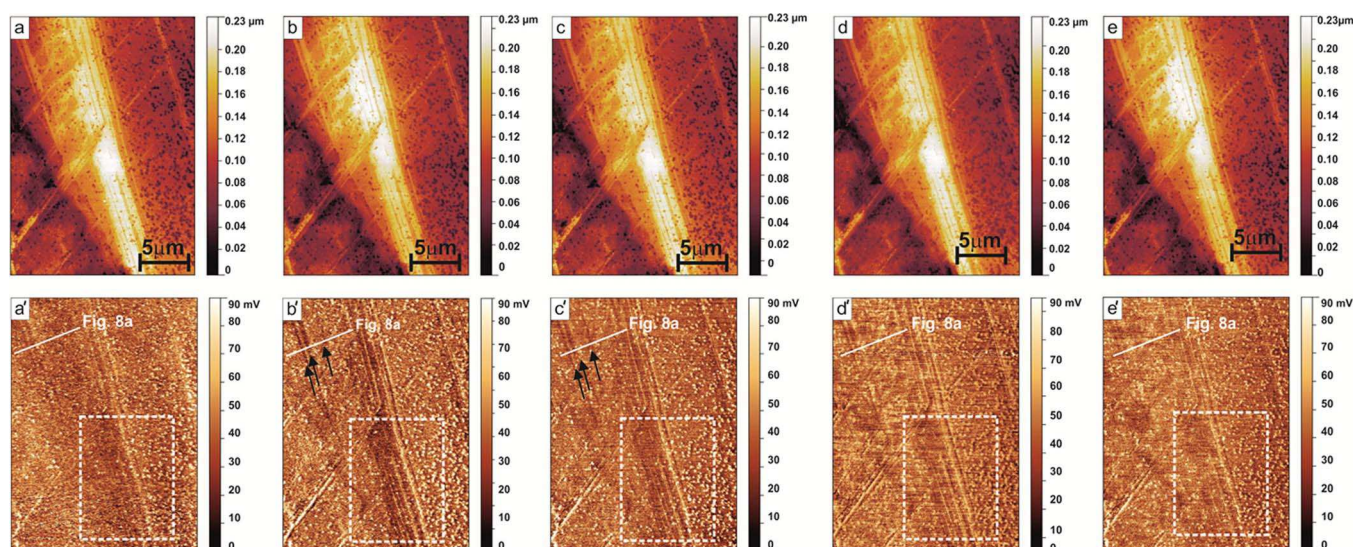
Figure 7. SKPFM results showing topographic and potential images taken at exposure times of (a, a′) 6, (b, b′) 67, (c, c′) 168, (d, d′) 235, and (e, e′) 300 hours. SKPFM: Scanning Kelvin Probe Force Microscopy. The dark color indicates a relatively low potential which corresponds to a higher hydrogen content compared to other locations. Accordingly, the bright contrast indicates a relatively high potential, in other words, lower hydrogen content. A corresponding calibration curve was published in the previous paper.[34]
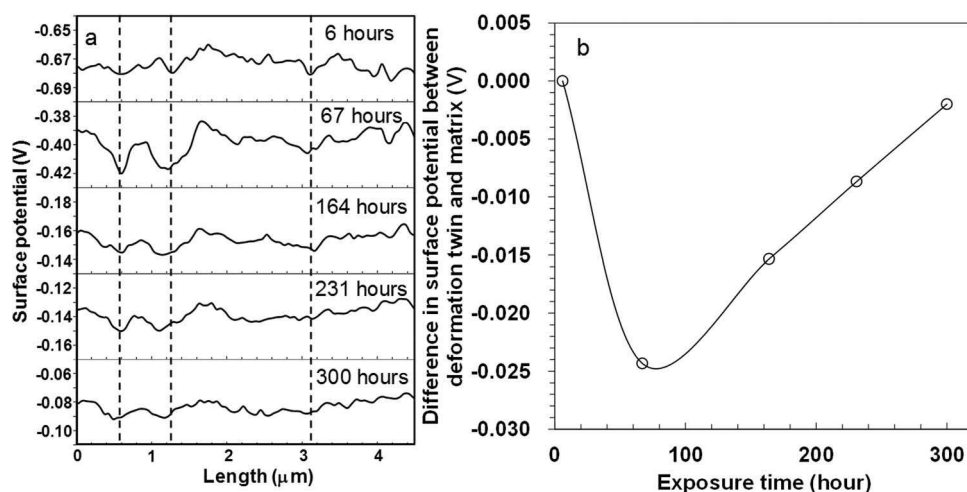

Figure 8. (a) Line profiles of surface potential corresponding to the white lines in Figs. 7a′–7e′. (b) The difference of potential between twin and average potential in the line profile. The potential at twin was defined as average of the minimum potentials of the respective twins shown in Fig. 8a.

such as Σ3 indicates a geometrically highly coincident interface. It should be emphasized though that the full coherency and segregation state of an interface requires also the interface plane to be considered. When observed first, twin boundary cracking was considered an unexpected phenomenon in FCC alloys, since the Σ3 twin boundary is often coherent, depending on its interface plane inclination, and was hence assumed to have only a weak interaction with hydrogen.[10] Therefore, in this study, we discuss the local hydrogen segregation and boundary cracking behavior through the analyses of the present results.

Hydrogen trapping ability and desorption behavior.— The activation energies of 30 and 32 kJ·mol^{-1} correspond to hydrogen detrapping from dislocations and micro-voids.[12,38,45] Also, these peaks could include hydrogen desorption from interstitial sites, vacancies, and grain boundaries, which show similar or slightly lower activation energies than dislocations.[38] Since the first and second peaks completely disappeared after the exposure to air for 300 h, the hydrogen trapped in these sites is concluded to be diffusible at room temperature.
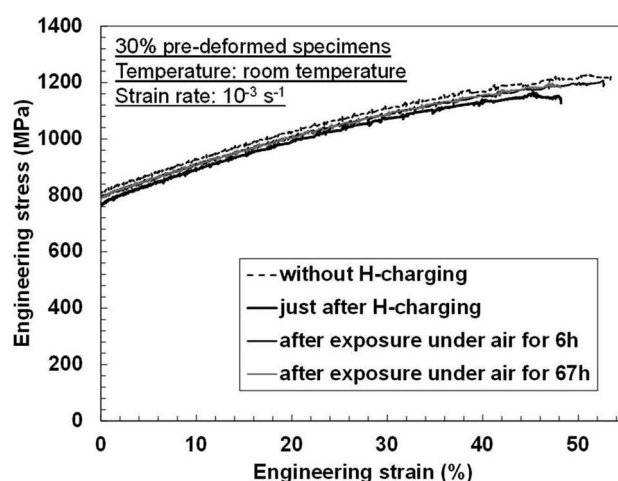

Figure 9. Engineering stress-strain curves for the various sample conditions.
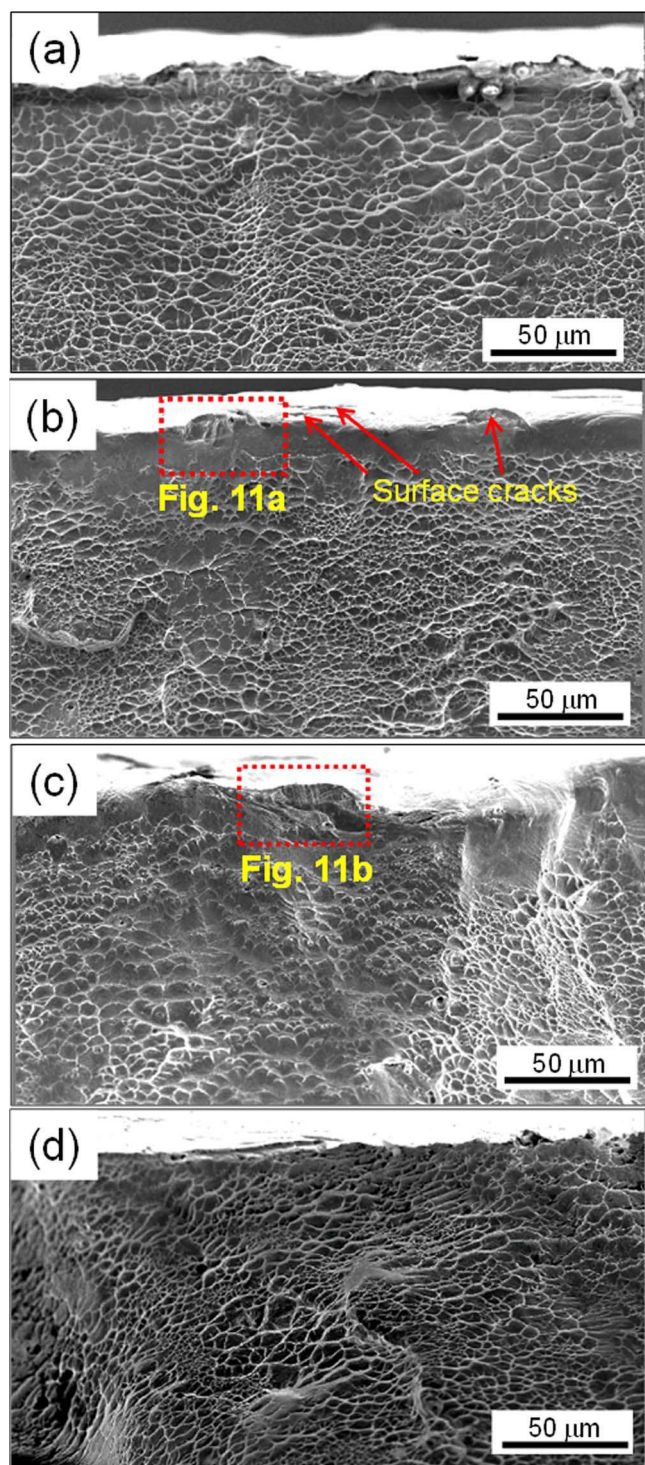
Figure 10. Fractographs of the specimens (a) without hydrogen-charging, (b) immediately after hydrogen charging, (c) after exposure to air for 6 h, and (d) after exposure to air for 67 h.

Figure 11. Magnified images of the regions outlined by the red broken lines in (a) Fig. 10b and (b) Fig. 10c.

and fifth peaks.[48,49] Hence, the fourth and fifth peaks are considered to stem from hydrogen detrapping from dislocation cores or MnS inclusions. The peak heights of the fourth and fifth peaks increased with longer air exposure time. The reason why the peak height increased is seen in hydrogen transfer from reversible trap sites to irreversible trap sites. Some of the weekly trapped hydrogen diffuses to irreversible hydrogen trap sites and cannot easily escape from them at room temperature. Thus, the cumulative hydrogen content represented by the fourth and fifth peaks increased with longer air exposure time through such a hydrogen transfer mechanism.

The intermediate activation energy of 58 kJ·mol^{-1} obtained for the third peak corresponds to the hydrogen detrapping from twin boundaries.[12] A strong indicator for this is that this intermediate activation energy was not observed in other austenitic steels which do not contain deformation twins e.g. κ-carbide hardened austenitic steel with a high stacking fault energy.[4,50] As shown in Fig. 5, the third peak height hardly changes even after exposure to air for 6 h, and only very slowly decayed and approached the level observed for the hydrogen-uncharged condition after air exposure for 300 h. Additionally, the cumulative hydrogen content observed for the third peak is remarkably lower than the other peaks. These facts indicate that the hydrogen detrapping rate from twin boundaries is lower than that from typical diffusible hydrogen trap sites, and the reduction in the third peak height after the air exposure for 300 h indicates that the hydrogen on twin boundaries is more active than that in irreversible hydrogen trap sites shown as fourth and fifth peaks in Fig. 5a. It is unlikely that the coherent portions of the $\Sigma 3$ twin boundaries can act as hydrogen trap sites,[10] however, the incoherent regions of the same twin boundaries can indeed act as a highly efficient trap sites.[3] The importance of locally incoherent misfit regions on otherwise coherent twin boundaries has been reported for the case of interstitial carbon segregation in iron studied by atom probe tomography.[51] Moreover, autoradiography in an austenitic stainless steel has clarified that hydrogen segregates at facet corners on twin boundaries.[52,53] The facet corners are actually produced by dislocation-twin interactions. Dislocations intersect twin boundaries through a dislocation dissociation mechanism.[54,55] For instance,[54]

$$1/2[\bar{1}01](111) \rightarrow 1/6[\bar{1}14](\bar{5}\bar{1}\bar{1}) + 1/6[\bar{2}\bar{1}\bar{1}](\bar{1}11) \qquad [2]$$

On the other hand, the activation energies of 71 and 80 kJ·mol^{-1} obtained for the fourth and fifth peaks would correspond to hydrogen detrapping from dislocation cores,[46] precipitates or inclusions which are known to be irreversible trap sites. An activation energy of 72 kJ·mol^{-1} for mixed dislocation cores was also reported by Li, Gangloff and Scully.[47] In the present steel, only MnS (shown in Figs. 12a′ and 12d′) could be a possible precipitate or inclusion type which might lead to the large cumulative hydrogen content revealed by the fourth
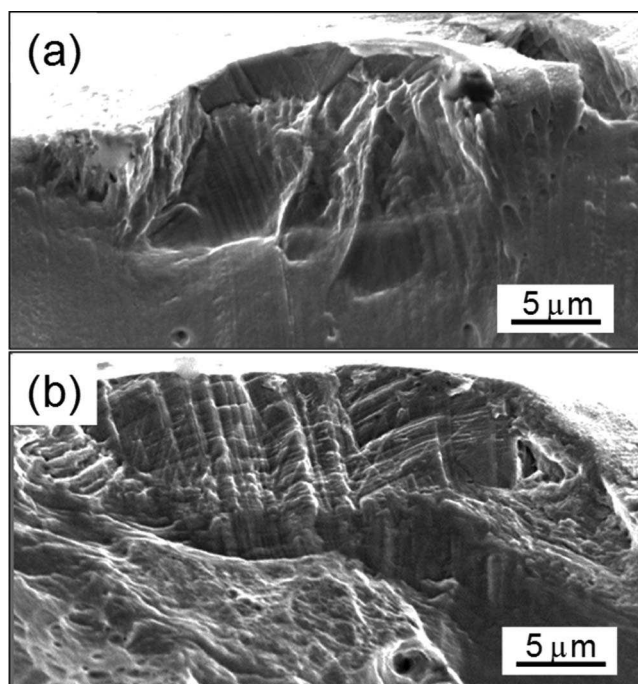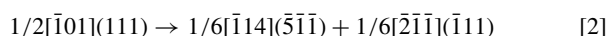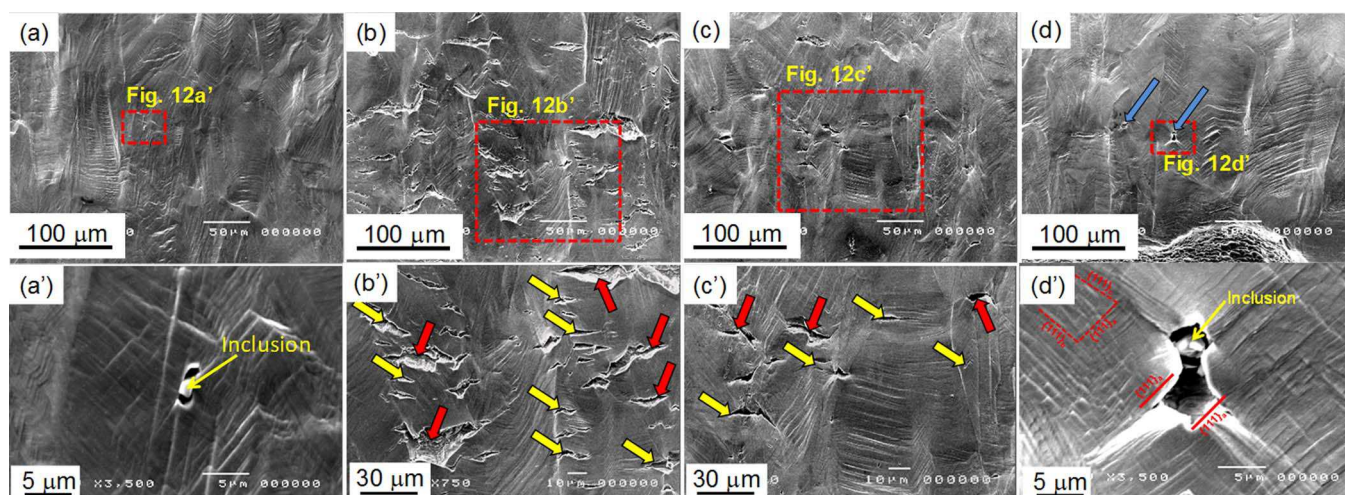
Figure 12. Surface (//ND) condition at vicinities of the fracture parts of the specimens (a) without hydrogen-charging, (b) just after hydrogen charging, (c) after exposure to air for 6 h, and (d) after exposure to air for 67 h. (a′)-(d′) Magnified images of the regions outlined by the red broken line in each image.

where the $(\bar{1}11)$ plane is the obstacle twin boundary. The formation of $1/6[\bar{2}\bar{1}1]$ dislocations creates slip steps on the obstacle twin boundary,[56] resulting in the facet corners. Thus, twin boundaries in deformed TWIP steels such as the present specimen include a considerable amount of facet corners. The numerous facet corner forms the curved twin boundaries shown in Fig. 7. Therefore, it is plausible that the cumulative hydrogen content on twin boundaries is essentially smaller than that in the other trap sites. However, the local hydrogen content on such interfaces at the incoherent portions may be very high, promoting initiation of embrittlement. A more detailed discussion of this effect is given in the next section.

Hydrogen distribution.— Dislocations, vacancies and interstitial positions are preferred sites for diffusible hydrogen.[12,44,45,57] Presence of the diffusible hydrogen in such defects was demonstrated via Kissinger analysis on the first and second peaks in the TDA results. Higher densities of such defects exist at deformation twins compared to the surrounding matrix.[36] However, the relatively slow buildup of the potential contrast with increasing exposure time (after 67 h exposure in dry nitrogen) raises questions whether this phenomenon can indeed be correlated to hydrogen desorption from such sites. Even after air exposure for 6 h, the first peak disappeared, and the height of the second peaks decreased steeply as shown in Fig. 5b. Since the sample handling also takes some time, i.e. through the palladium evaporation after hydrogen loading, mounting the sample in the SKPFM and starting the measurement we, therefore, conclude that the hydrogen that leads to the relatively slow development of the observed potential contrast originates from trap sites with a lower hydrogen desorption rate, e.g. twin boundaries.

As revealed in Fig. 7b′, the dark area in the potential images indeed appeared clearly at deformation twins with a maximum contrast to the matrix after an exposure time of 67 hours. First it should be noted that the hydrogen charging time in the present study is very short and, accordingly, the depth of the hydrogen-affected zone is shallow. A diffusion coefficient of hydrogen in a non-deformed TWIP steel has been reported to be about 1×10^{-13} m$^2 \cdot$ s^{-1}.[58] Assuming that the diffusion coefficient is similar for this TWIP steel, the depth of the hydrogen-affected zone is estimated to be about 20 μm by using $(Dt)^{1/2}$ criterion where D is diffusion coefficient of hydrogen, and t is hydrogen-charging time. In fact, deformation-induced lattice defects suppress hydrogen diffusion, e.g. 10% cold rolling in steel decreased the diffusion coefficient by a factor of 10 compared to that of the as-annealed condition.[59] Considering the reduction of the diffusion coefficient by a factor of 10, the depth of the hydrogen-affected zone is estimated to be certainly below 10 μm in the present hydrogen-charging condition. Since the average grain size and the thickness

of twin plates in the 30%-deformed condition are about 50 and 1–3 μm, respectively,[3] the depth of the hydrogen-affected zone roughly corresponds to the twin thickness, and is smaller than the grain size. Hence, under the chosen charging conditions, it was assumed that contrast between hydrogen available at the twin in comparison to the matrix within the grains should be well resolvable. In fact, the resolution of the features that can be seen in Fig. 7 seems to be even better than 3 μm. This is attributed to the fact that most of the hydrogen located originally in the dominant, i.e. shallow sites, that would lead to smearing out of contrast, has already left the surface region when the SKPFM measurements start after about 1–1.5 hours after hydrogen loading. Thus, the influence of hydrogen release from twin boundaries seems to play the dominant role during the here observed later stages, owing to the higher activation energy for hydrogen desorption from twins. A further reason for the the high localization at of the hydrogen release into the Pd film is most likely a preferred hydrogen transport along the twin boundaries (as compared to through the matrix).

Since a reduction in potential is related to relatively high hydrogen concentration in the palladium layer, the first increasing dark contrast at the twin boundaries indicates an increasingly higher accumulation of hydrogen in the palladium over the twins than over the matrix (see Figs. 7a′–7b′). Deformation twins in such steels actually consist of twin/matrix bundles,[11,36,37] providing a nanolamellar morphology such as observed in the topographic and potential images outlined by the white dotted area depicted in Fig. 7. The contrast detected by the Kelvin probe experiment is maintained as long as hydrogen is desorbed significantly from twin boundaries compared to the matrix. The sequence of images shown in Fig. 7 reveals that the overall signal difference indicating local hydrogen desorption from twins compared to matrix desorption is weak and does not last very long. This relatively small potential difference means that the relative difference in hydrogen release rate from the twin boundaries is quite small compared to that from the matrix at the observed stage (a few hours after hydrogen charging where the shallowly bound hydrogen has already left the surface near region). As hydrogen at twins is relatively weakly bound[10] (although clearly stronger than diffusible hydrogen in the adjacent undefected matrix[12]), that also means that the most likely the overall concentration there will be relatively low, because otherwise a larger relative release rate would be expected. Hence, the extra hydrogen from the twin boundaries is also relatively quickly exhausted, and the contrast decreases again due to the general near-logarithmic decrease in potential due to the slowly but steadily increasing hydrogen concentration in the palladium film[26,33,34] stemming from the background of continuous hydrogen release from the statistically distributed deeper trap sites.[26,34]
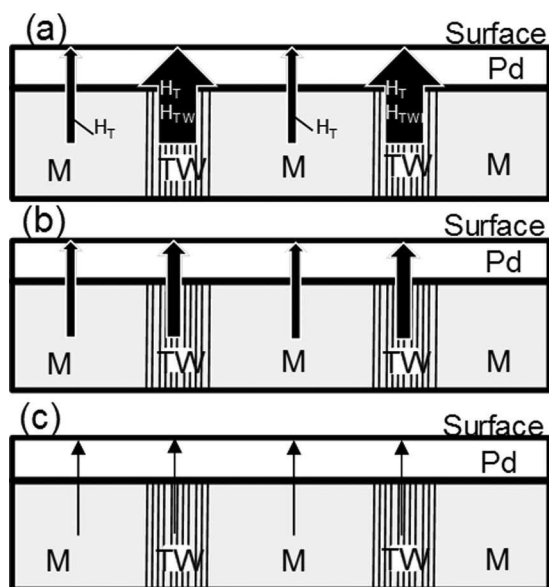
Figure 13. Schematics about the correlation between local hydrogen desorption and the associated change in surface potential as detected by Scanning Kelvin Probe Force Microsocpy (SKPFM). The thickness of the arrows expresses the amount of hydrogen schematically. The symbols H_{TW}, and H_T indicate hydrogen stored at traps sites such as twins and other positions, respectively. M: Matrix. T: Twin.

The interpretation of the SKPFM results in the heterogeneous microstructure is schematically summarized in Fig. 13. Since interstitial sites, vacancies, vacancy clusters, and dislocations are dominant low energy trap sites for hydrogen compared to twin boundaries,[12] these hydrogen atoms are desorbed first, probably in part already during sample handling, before the first measurement can be recorded. These weakly bonded hydrogen atoms are taken up by the palladium film and react with oxygen from the environment during the initial stages of sample handling. Thus, the first actual measurements are recorded from a palladium film where diffusible hydrogen is depleted due to the H_2O formation on the surface. This initial stage corresponds to the line profiles taken after 6 hours as shown in Fig. 8a. In contrast, hydrogen desorption from twin boundaries proceeds over a longer time scale compared to interstitial, dislocation and vacancy related hydrogen desorption (Fig. 13a). This effect produces the contrast in the potential image and the peaks on the line profiles after an exposure for 67 hours as shown in Fig. 8a. After that, the hydrogen desorption rate from twin boundaries also drops (Fig. 13b), and hence the concentration of hydrogen accumulating in the palladium film above the matrix is catching up, reducing the contrast in the potential image and smoothing the line profiles again. Hence, the potential image became sharper with time up to 67 h, and then, more blurred with further exposure time as shown in Figs. 8a and 8b. Finally the difference in potential disappears when the concentration in the palladium layer above the matrix has caught up and hydrogen desorption is only due to slow release from deeper traps (Fig. 13c). The existence of hydrogen on twin boundaries, specifically on their less coherent portions, and its diffusivity at room temperature explain the hydrogen-assisted twin boundary cracking that was observed in previous works,[3,18–21] underlining that the diffusible hydrogen at room temperature plays indeed a key role for hydrogen embrittlement.[57] However, it should be noted that fully coherent $\Sigma 3$ twin boundaries with a fully coherent interface plane orientation cannot plausibly act as a deep hydrogen trap site.[10] Instead, it is assumed that only incoherent portions of these twin boundaries (e.g. facet corner on twin boundaries[52,53]) that are distorted or slightly tilted out of the fully coherent interface plane can act as deep hydrogen traps as discussed in section Hydrogen trapping ability and desorption behavior. Such a profound difference in interstitial trapping between coherent and less coherent twin bound-

ary regions was recently proven for a Fe-C system, where already deviations above ~4° from full $\Sigma 3$ coherency substantially increased the solubility for carbon.[51] This observation supports that specifically incoherent twin interface portions, secondary grain boundary dislocations and / or secondary deformation twins may indeed act as efficient trapping sites for hydrogen storage in the present material.[3] The interaction of this locally very high hydrogen content stored at a small incoherent portion of a twin boundary is assumed to efficiently promote hydrogen-assisted cracking at such sites.

Hydrogen-assisted cracking.— No difference was observed among the stress-strain curves taken after different air exposure times. This is attributed to two factors: the relatively high strain rate and the shallow hydrogen-affected zone. The former factor is associated with hydrogen localization at a crack tip[60,61] and hydrogen/dislocation competitive motion associated with hydrogen-enhanced localized plasticity.[62–64] Therefore, a hydrogen-effect may appear at a lower strain rate than that used for the present tests. The latter factor is related to the fact that hydrogen cannot diffuse to deeper portions inside of the specimen after only 30 min due to the low diffusion coefficient of hydrogen in the austenitic phase. More specifically, the depth of the hydrogen-affected zone was estimated to be well below 10 μm as mentioned above. Nevertheless, the fracture surface observed in the vicinity of the sample surface as well as the surface cracks showed important features depending on the respective air exposure times. In fact, it has been reported that only a small difference in the stress-strain responses is observed when the hydrogen charging time is not sufficient for loading and sweeping also the entire bulk region of a TWIP steel, but only the surface region.[16] Brittle cracking occurs only in the hydrogen-affected zone, and the high ductility capacity of the present steel is considered to suppress propagation of such shallow cracks. Since the fracture surface was totally ductile in the hydrogen-uncharged specimen, the brittle cracking shown in Fig. 11 stems from hydrogen uptake. Also here note that the depth of the area showing the brittle cracking almost was 4–10 μm, which reasonably corresponds to the estimated depth of the hydrogen-affected zone.

As shown in Figs. 12b′ and 12c′, some of the near-surface cracks were located along or parallel to deformation twin boundaries, indicating that twin boundary cracking occurred. $\Sigma 3$ twin boundaries are usually resistant to brittle cracking in cases without any hydrogen charging. However, when probed at low temperature conditions or when ε-martensite forms,[65,66] $\Sigma 3$ twin boundaries were indeed observed to crack. These facts indicate that $\Sigma 3$ twin boundaries can indeed crack when assisted by an additional factor i.e. hydrogen segregation as in the present case. Therefore, hydrogen must exist on twin boundaries to some extent to assist cracking at ambient temperatures in the present TWIP steel. Also note that hydrogen-assisted intergranular cracking was observed as the major cracking mode in the condition immediately after the hydrogen-charging, but the dominancy was decreased with time compared to the twin boundary cracking as shown in Figs. 12b′ and 12c′. This fact indicates that grain boundary can trap a significant amount of hydrogen, but was desorbed faster than twin boundaries. As indicated by the TDS and SKPFM results discussed above, hydrogen actually does exist on the incoherent portions of the twin boundaries, and remains there for longer times than at the other diffusible hydrogen trap sites. As a result, hydrogen-assisted twin boundary cracking occurred, and was relatively promoted with time compared to the intergranular cracking. Since hydrogen on twin boundaries is also diffusible at ambient temperature, the surface cracking along such twin boundaries was gradually suppressed with increasing the air exposure time. Because most hydrogen was desorbed from the diffusible hydrogen trap sites after air exposure for 300 h, the brittle cracking disappeared completely after exposure to air for 300 h. However, even after 300 h, some remaining hydrogen seems to affect the slip behavior as indicated by Fig. 12d′. This could be caused by the remaining hydrogen around inclusions as shown in the TDA profile, since intense slip lines appeared around the ductile void that occurred in the vicinity of inclusions.

Conclusions

A Scanning Kelvin Probe Force Microscopy approach was successfully used to detect hydrogen in deformation twin plates in an Fe-Mn-C austenitic TWIP steel with high spatial resolution. The hydrogen content stored at deformation twins remains longer in the material than diffusible hydrogen in interstitial sites, vacancies and dislocations, yet, shows significant mobility at room temperature. These facts were supported by thermal desorption analysis as well as observations of surface cracking behavior of hydrogen-charged specimens after different air exposure times after the hydrogen charging. We suggest that hydrogen localization at deformation twins assists hydrogen-induced twin boundary cracking. The novel Scanning Kelvin Probe Force Microscopy approach presented here solves two main challenges associated with the investigation of hydrogen embrittlement, namely, the detection of hydrogen with high local and chemical sensitivity and the microstructure-dependent and spatially resolved observation of the kinetics of hydrogen desorption.

Acknowledgments

References

1. Y. Oda and H. Noguchi, *International Journal of Fracture*, **132**, 99 (2005).
2. T. Michler and J. Naumann, *International Journal of Hydrogen Energy*, **35**, 1485 (2010).
3. M. Koyama, E. Akiyama, K. Tsuzaki, and D. Raabe, *Acta Mater*, **61**, 4607 (2013).
4. M. Koyama, H. Springer, S. V. Merzlikin, K. Tsuzaki, E. Akiyama, and D. Raabe, *International Journal of Hydrogen Energy*, **39**, 4634 (2014).
5. M. Koyama, E. Akiyama, and K. Tsuzaki, *Scripta Mater*, **66**, 947 (2012).
6. D. Abraham and C. Altstetter, *Metallurgical and Materials Transactions A*, **26**, 2859 (1995).
7. D. G. Ulmer and C. J. Altstetter, *Acta Metallurgica et Materialia*, **39**, 1237 (1991).
8. M. Koyama, C. C. Tasan, E. Akiyama, K. Tsuzaki, and D. Raabe, *Acta Mater*, **70**, 174 (2014).
9. K. Takai, J. Seki, and Y. Homma, *Materials Transactions, JIM*, **36**, 1134 (1955).
10. Y. A. Du, L. Ismer, J. Rogal, T. Hickel, J. Neugebauer, and R. Drautz, *Phys Rev B*, **84** (2011).
11. D. R. Steinmetz, T. Jäpel, B. Wietbrock, P. Eisenlohr, I. Gutierrez-Urrutia, A. Saeed-Akbari, T. Hickel, F. Roters, and D. Raabe, *Acta Mater*, **61**, 494 (2013).
12. K. H. So, J. S. Kim, Y. S. Chun, K. T. Park, Y. K. Lee, and C. S. Lee, *Isij Int*, **49**, 1952 (2009).
13. M. Koyama, T. Sawaguchi, T. Lee, C. S. Lee, and K. Tsuzaki, *Materials Science and Engineering A*, **528**, 7310 (2011).
14. M. Koyama, T. Sawaguchi, and K. Tsuzaki, *Isij Int*, **53**, 323 (2013).
15. M. Koyama, E. Akiyama, and K. Tsuzaki, *Corros Sci*, **54**, 1 (2012).
16. J. A. Ronevich, S. K. Kim, J. G. Speer, and D. K. Matlock, *Scripta Mater*, **66**, 956 (2012).
17. Y. S. Chun, K. T. Park, and C. S. Lee, *Scripta Mater*, **66**, 960 (2012).
18. M. Koyama, E. Akiyama, T. Sawaguchi, D. Raabe, and K. Tsuzaki, *Scripta Mater*, **66**, 459 (2012).
19. J. H. Ryu, S. K. Kim, C. S. Lee, D.-W. Suh, and H. K. D. H. Bhadeshia, *Proceedings of the Royal Society A: Mathematical, Physical and Engineering Science*, **469** (2013).
20. M. Koyama, E. Akiyama, T. Sawaguchi, K. Ogawa, I. V. Kireeva, Y. I. Chumlyakov, and K. Tsuzaki, *Corros Sci*, **75**, 345 (2013).
21. T. Michler, C. San Marchi, J. Naumann, S. Weber, and M. Martin, *International Journal of Hydrogen Energy*, **37**, 16231 (2012).
22. T. E. Pérez and J. Ovejero García, *Scripta Metall Mater*, **16**, 161 (1982).
23. J. Ovejero-García, *J Mater Sci*, **20**, 2623 (1985).
24. H. K. Yalçi and D. V. Edmonds, *Mater Charact*, **34**, 97 (1995).
25. S. Kühn, F. Unterumsberger, T. Suter, and M. Pohl, *Materials Testing*, **55**, 648 (2013).
26. S. Evers, C. Senöz, and M. Rohwerder, *Sci Technol Adv Mat*, **14**, 014201 (2013).
27. G. Williams, H. N. McMurray, and R. C. Newman, *Electrochem Commun*, **27**, 144 (2013).
28. R. F. Schaller and J. R. Scully, *Electrochem Commun*, **40**, 42 (2014).
29. C. Larignon, J. Alexis, E. Andrieu, L. Lacroix, G. Odemer, and C. Blanc, *Scripta Mater*, **68**, 479 (2013).
30. C. Senöz, S. Evers, M. Stratmann, and M. Rohwerder, *Electrochem Commun*, **13**, 1542 (2011).
31. M. Rohwerder and F. Turcu, *Electrochim Acta*, **53**, 290 (2007).
32. S. Evers, C. Senöz, and M. Rohwerder, *Electrochim Acta*, **110**, 534 (2013).
33. R. Kirchheim and R. B. McLellan, *J Electrochem Soc*, **127**, 2419 (1980).
34. S. Evers and M. Rohwerder, *Electrochem Commun*, **24**, 85 (2012).
35. M. Koyama, M. Murakami, K. Ogawa, T. Kikuchi, and T. Sawaguchi, *Mater Trans*, **49**, 812 (2008).
36. H. Idrissi, K. Renard, L. Ryelandt, D. Schryvers, and P. J. Jacques, *Acta Mater*, **58**, 2464 (2010).
37. I. Gutierrez-Urrutia and D. Raabe, *Acta Mater*, **59**, 6449 (2011).
38. W. Y. Choo and J. Lee, *Metallurgical Transactions A*, **13**, 135 (1982).
39. I. Gutierrez-Urrutia and D. Raabe, *Scripta Mater*, **66**, 992 (2012).
40. R. Hausbrand, M. Stratmann, and M. Rohwerder, *J Electrochem Soc*, **155**, C369 (2008).
41. D. K. Han, Y. M. Kim, H. N. Han, H. K. D. H. Bhadeshia, and D.-W. Suh, *Scripta Mater*, **80**, 9 (2014).
42. M. Koyama, E. Akiyama, and K. Tsuzaki, *Isij Int*, **53**, 1089 (2013).
43. M. Koyama, E. Akiyama, and K. Tsuzaki, *Isij Int*, **53**, 1268 (2013).
44. M. Koyama, E. Akiyama, and K. Tsuzaki, *Corros Sci*, **59**, 277 (2012).
45. S. Frappart, A. Oudriss, X. Feaugas, J. Creus, J. Bouhattate, F. Thébault, L. Delattre, and H. Marchebois, *Scripta Mater*, **65**, 859 (2011).
46. S. Taketomi, R. Matsumoto, and N. Miyazaki, *Acta Mater*, **56**, 3761 (2008).
47. D. Li, R. Gangloff, and J. Scully, *Metallurgical and Materials Transactions A*, **35**, 849 (2004).
48. J. L. Lee and J. Y. Lee, *Met Sci*, **17**, 426 (1983).
49. S. Hong, S. Y. Shin, H. S. Kim, S. Lee, S.-K. Kim, K.-G. Chin, and N. J. Kim, *Metallurgical and Materials Transactions A*, **44**, 776 (2012).
50. M. Mizuno, H. Anzai, T. Aoyama, and T. Suzuki, *Materials Transactions, JIM*, **35**, 703 (1994).
51. M. Herbig, D. Raabe, Y. J. Li, P. Choi, S. Zaefferer, and S. Goto, *Phys Rev Lett*, **112** (2014).
52. H. Saito, K. i. Miyazawa, and Y. Ishida, *Nippon Kinzoku Gakkaishi/Journal of the Japan Institute of Metals*, **55**, 366 (1991).
53. H. Saito, M. Mori, and Y. Ishida, *Nippon Kinzoku Gakkaishi/Journal of the Japan Institute of Metals*, **59**, 910 (1995).
54. S. Mahajan and G. Y. Chin, *Acta Metall Mater*, **21**, 173 (1973).
55. L. Rémy, *Acta Metall Mater*, **25**, 711 (1977).
56. Y. B. Wang and M. L. Sui, *Appl Phys Lett*, **94**, 021909 (2009).
57. K. Takai and R. Watanuki, *Isij Int*, **43**, 520 (2003).
58. S. K. Kim, P. Y. Oh, S.-H. Jeon, S. H. Han, S. E. Kang, and K.-G. Chin, in *Steely hydrogen conference* (2011).
59. H. Hagi and Y. Hayashi, *T Jpn I Met*, **28**, 368 (1987).
60. P. Sofronis and R. M. McMeeking, *Journal of the Mechanics and Physics of Solids*, **37**, 317 (1989).
61. D. Sasaki, M. Koyama, K. Higashida, K. Tsuzaki, and H. Noguchi, *International Journal of Hydrogen Energy*, **40**, 9825 (2015).
62. J. Tien, A. Thompson, I. M. Bernstein, and R. Richards, *Metallurgical Transactions A*, **7**, 821 (1976).
63. S. Taketomi, R. Matsumoto, and N. Miyazaki, *J Mater Res*, **26**, 1269 (2011).
64. D. Sasaki, M. Koyama, S. Hamada, and H. Noguchi, *Phil Mag Lett*, **95**, 260 (2015).
65. M. Koyama, T. Sawaguchi, and K. Tsuzaki, *Isij Int*, **52**, 161 (2012).
66. M. Koyama, T. Sawaguchi, and K. Tsuzaki, *Metallurgical and Materials Transactions A: Physical Metallurgy and Materials Science*, **43**, 4063 (2012).